Low-temperature magnetism and crystal field effects in the triangular-lattice delafossites $TlErSe_2$ and $TlTmSe_2$

Bastian Rubrecht,[1] Ellen Häußler,[2] Mirtha Pillaca,[2] Pritam Bhattacharyya,[3] Liviu Hozoi,[3] Artem Nosenko,[1,4] Dmitri V. Efremov,[1] Bernd Büchner,[1,5] Anja U. B. Wolter,[1] and Thomas Doert[2]

[1]*Institute for Solid State Research, Leibniz IFW Dresden, Helmholtzstraße 20, 01069 Dresden, Germany*

[2]*Faculty of Chemistry and Food Chemistry, Technische Universität Dresden, 01062 Dresden, Germany*

[3]*Institute for Theoretical Solid State Physics, Leibniz IFW Dresden, Helmholtzstraße 20, 01069 Dresden, Germany*

[4]*Department of Theoretical and Mathematical Physics, Kyiv Academic University, 03142 Akademika Vernads'koho Boulevard, 36, Kyiv, Ukraine*

[5]*Institute of Solid State and Material Physics and Würzburg-Dresden Cluster of Excellence ct.qmat, Technische Universität Dresden, 01062 Dresden, Germany*

(Received 15 December 2025; revised 13 August 2026; accepted 25 August 2026; published 3 November 2026)

Delafossite compounds containing rare-earth ions have been proven to be an ideal platform to investigate frustrated magnetic ground states. Here, we discuss two triangular-lattice antiferromagnets, $TlErSe_2$ and $TlTmSe_2$, as potential candidates for hosting exotic quantum states. Powder x-ray diffraction data analysis of the black polycrystalline $TlMSe_2$ (M: Er and Tm) samples confirms the phase purity. Both materials crystallize in the trigonal α-$NaFeO_2$ structure ($R\bar{3}m$) with lattice parameters $a = 4.1070(4)$ Å and $c = 23.1472(1)$ Å for the erbium compound and $a = 4.0916(1)$ Å and $c = 23.1483(2)$ Å for the thulium compound. Magnetic susceptibility measurements show an effective moment of $\mu_{\text{eff}} = 9.6(2)\mu_B$/f.u. ($7.5(1)\mu_B$/f.u.) for $TlErSe_2$ ($TlTmSe_2$) for temperatures above 200 K. While ^{3}He specific heat measurements reveal long-range magnetic order below $T_N = 0.42$ K for $TlErSe_2$, no sign of long-range magnetic order was observed for $TlTmSe_2$. Combining both experimental and computational results, we discuss the striking difference in the magnetic behavior of $TlTmSe_2$ and map out the T-H phase diagram for polycrystalline $TlErSe_2$.

DOI: 10.1103/sfns-yxpr

I. INTRODUCTION

Frustration lies at the heart of a variety of exotic magnetic ground states and responses in solid state magnetism. It can have a pure geometric nature like the Heisenberg antiferromagnetic triangular lattice or can arise from competing anisotropic interactions as in Kitaev's honeycomb model. In some systems it may actually imply both geometric frustration and peculiar anisotropic couplings, e.g., on triangular lattices of edge-sharing MX_6 octahedra, where M stands for a d- or f-electron ion and X stands for a chalcogen or halide species. Illustrative examples of such edge-sharing networks of MX_6 octahedra are triangular Kitaev-Heisenberg materials like the iridates [1], CoI_2 [2], $NaRuO_2$ [3], and $ACeX_2$ [4,5] (A: alkali metal) and Ising antiferromagnets with "intrinsic" transverse fields [6] like $TmMgGaO_4$ [7–10] and $KTmSe_2$ [11]. The former provide the playground for studying quantum spin liquid (QSL) physics [3]; the latter are of interest in relation to Berezinskii-Kosterlitz-Thouless (BKT) phases [12,13].

Rare-earth delafossites with the chemical formula AMX_2 emerge in this context as a versatile material platform that allows one to investigate both QSL and BKT states. Although the role of Kitaev exchange is not yet fully clarified in some cases, potential QSL ground states have been proposed for Kramers-ion-based systems such as Yb^{3+} $4f^{13}$ [14–24] and Ce^{3+} $4f^1$ [5]. On the other hand, structurally related compounds hosting non-Kramers ions with a $4f^{12}$ configuration, e.g., $TmMgGaO_4$, represent promising potential BKT systems [9,10,13]. Although such ions often exhibit singlet ground states, low-lying crystal electric field (CEF) excited states can give rise to magnetic degrees of freedom, in particular, pseudodoublet effective moments and intrinsic transverse fields [6].

Here, we report the synthesis and a detailed study of the low-temperature magnetic and thermodynamic properties of both odd- and even-electron compounds in the $4f^n$ AMX_2 delafossite series displaying the same ligand and A-site matrix: $TlErSe_2$ and $TlTmSe_2$. The former features $\tilde{S} = 1/2$ magnetic moments originating from the Er^{3+} $4f^{11}$ Kramers-doublet (KD) ground state and is found to order antiferromagnetically below 420 mK. No sharp phase transition is observed in the latter non-Kramers $4f^{12}$ material; its low-energy multiplet structure is discussed in light of recent reports on the realization of the transverse field Ising model in related compounds [9,10,13]. Our results add reference points within the landscape of late rare-earth triangular-lattice magnetic systems. Studies on $A = Tl$ delafossites, in particular, are scarce, likely due to the toxicity of thallium; besides early works focusing on structural aspects and limited to temperatures $T \geqslant 4.2$ K [25–27], only the magnetism of the $4f^{13}$ Kramers-ion systems

Published by the American Physical Society under the terms of the Creative Commons Attribution 4.0 International license. Further distribution of this work must maintain attribution to the author(s) and the published article's title, journal citation, and DOI.

$TlYbS_2$ [28] and $TlYbSe_2$ [24] has been addressed so far. Our work provides valuable insights into this particular topic.

II. EXPERIMENTAL AND COMPUTATIONAL METHODS

Synthesis. Due to the air and moisture sensitivity of the starting materials and products, all the experimental work was carried out in an Ar-filled glove box with O_2 and H_2O levels below 0.1 ppm. Polycrystalline $TlErSe_2$ and $TlTmSe_2$ samples were synthesized in two steps via the solid-state method by using high-purity elements of Tl (Alfa Aesar, 99.9%), erbium (Mateck, 99.5%), thulium (Mateck, 99.99%), and Se (Chempur, 99.999%, reduced in a H_2 stream at 400 °C) as raw materials.

First, the Tl_2Se precursor was synthesized from a 2 : 1 stoichiometric mixture of Tl and Se in an evacuated ($\sim 10^{-3}$ mbar) sealed quartz ampule. The ampule was placed in a muffle furnace (Nabertherm), heated up to 500°C with a ramp of 100 K/h, kept at this temperature for 24 h, and finally cooled down to room temperature within 5 h.

In the second step, polycrystalline $TlErSe_2$ and $TlTmSe_2$ were synthesized out of a stoichiometric mixture of Tl_2Se, Se, and Er or Tm, respectively. The three components were weighted in a molar ratio of 1 : 2 : 3, mixed in an agate mortar, and placed in a glassy-carbon crucible inside a quartz ampule 16 mm in diameter. The evacuated ampule was heated to 500 °C–540 °C with a heating rate of 100 K/h and kept at that temperature for 24 h. Afterward, the ampule containing $TlTmSe_2$ was cooled down by 10 K/h, and the ampule containing $TlErSe_2$ was water quenched. Both obtained samples were pulverized for further structural and physical property characterization.

In addition, a nonmagnetic reference material, $TlLuSe_2$, was synthesized in polycrystalline form following a similar procedure.

Powder x-ray diffraction. The phase purity of the prepared samples was checked by powder x-ray diffraction (PXRD) with an Empyrean diffractometer (PANalytical, Cu $K\alpha_1$ radiation) equipped with a Ge(111) monochromator. The data were collected in a Bragg-Brentano setup in the 2θ range of 5° to 90°. For an accurate lattice parameter measurement, the samples were mixed with a small amount of Si powder (NIST SRM 640*c*, $a = 5.43119(1)$ Å) as an internal standard. Lattice parameters of the samples were determined by Rietveld refinement using the TOPAS ACADEMIC software [29,30].

Magnetization and heat capacity. Magnetization and specific heat measurements were performed on pressed pellets of the polycrystalline sample. DC magnetometry was performed using a superconducting quantum interference device magnetometer from Quantum Design (MPMS3) for fields up to 7 T and a physical property measurement system (PPMS) for magnetic fields up to 14 T, both equipped with a vibrating sample magnetometer option.

The specific heat was measured using the relaxation method with a PPMS equipped with a ^{3}He refrigerator option. The background signal of the sample holder was measured separately and then subtracted. The lattice contribution to the specific heat was approximated by the Lindeman-scaled isostructural nonmagnetic analog $TlLuSe_2$.

Band structure density-functional computations. First-principles density-functional calculations were performed using the projector augmented-wave method [31], as implemented in the Vienna Ab initio Simulation Package (VASP) [32,33]. An energy cutoff of 700 eV was applied to the plane-wave basis set. The Brillouin zone was sampled using a Γ-centered $28 \times 28 \times 28$ k-point mesh. Spin-orbit coupling (SOC) was included self-consistently in all calculations. The f electrons of Er and Tm were treated as core electrons. For both compounds the trigonal crystal structure (space group 166) together with the experimentally obtained lattice parameters were used. The crystal structure parameters are $a = 4.0916(1)$ Å and $c = 23.1483(2)$ Å for $TlTmSe_2$ and $a = 4.1070(4)$ Å and $c = 23.1472(1)$ Å for $TlErSe_2$. All calculations assumed nonmagnetic configurations. For post-processing we used the PYMATGEN PYTHON library [34].

Quantum chemical calculations. *Ab initio* wave function quantum chemical calculations for the multiplet structures of both compounds, $TlErSe_2$ and $TlTmSe_2$, were carried out using the ORCA [35,36] and MOLPRO [37] programs, respectively. Clusters consisting of one central $ErSe_6$ ($TmSe_6$) octahedron, six adjacent Er (Tm) sites, and 12 Tl nearest-neighbor cations were considered. The crystalline environments were modeled as large arrays of point charges which reproduce the crystalline Madelung field within the cluster volume; we employed the EWALD program [38,39] to generate the point-charge embeddings. The performance of such an embedded-cluster quantum chemical approach for the case of $4f$-electron compounds is discussed in, e.g., [40,41].

The quantum chemical investigation was initiated as complete active space self-consistent field (CASSCF) computations [42] with active orbital spaces containing the seven $4f$ orbitals of the central Er or Tm ion. Post-CASSCF calculations were performed for the $TlTmSe_2$ system at the level of multireference configuration interaction (MRCI) with single and double excitations [42,43] out of the Tm $4f$ and Se $4p$ orbitals of the central $TmSe_6$ octahedron. The spin-orbit (SO) interaction matrix was computed for the lowest 11 spin triplet (out of a total of 21) and 9 spin singlet (out of a total of 28) $4f^{12}$ states. Other higher-lying triplet and singlet $4f^{12}$ states have relative energies that are, respectively, larger by $\sim$1 and $\sim$2.4 eV in the calculation without SOC; excluding those from the SO treatment does not significantly affect the low-energy $4f^{12}$ relativistic spectrum in $TlTmSe_2$, as illustrated at the CASSCF level in the Appendix (Table VI).

With three holes in the $4f$ subshell, MRCI is computationally too expensive for the $TlErSe_2$ compound. Post-CASSCF calculations were therefore performed for $TlErSe_2$ at the level of N-electron valence second-order perturbation theory (NEVPT2) [44]. All possible states (35 quartets and 112 doublets) derived from the $4f^{11}$ valence configuration were included in the SO treatment at either the CASSCF or NEVPT2 level. The basis sets used in the computational study are described in the Appendix.

III. RESULTS

The powder x-ray diffraction pattern based Rietveld analysis, shown in Fig. 1, confirms the single-phase formation of the polycrystalline $TlErSe_2$ and $TlTmSe_2$ compounds with

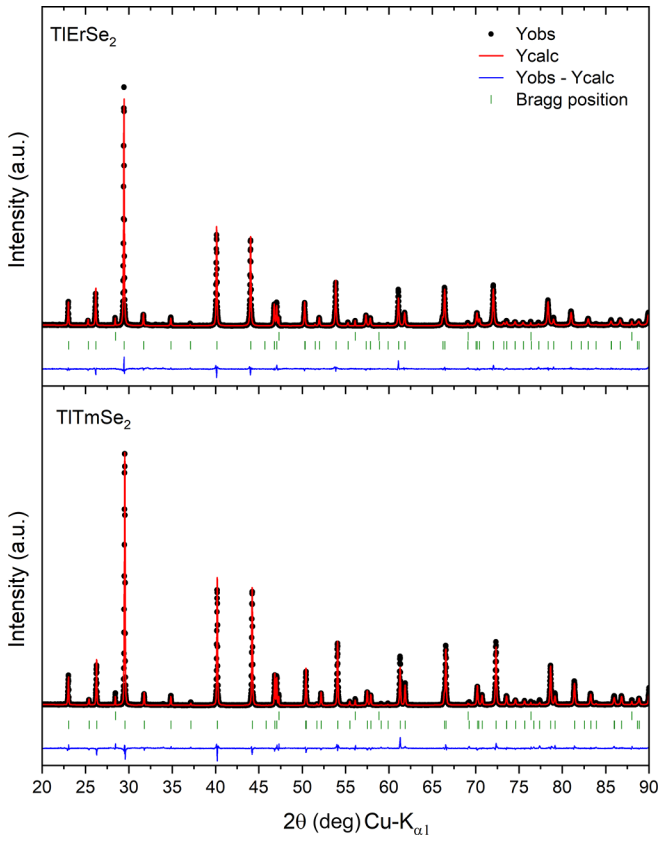


FIG. 1. PXRD pattern with Rietveld refinement analysis for $TlErSe_2$ (top) and $TlTmSe_2$ (bottom) samples. Solid black circles are observed intensities, red lines are the calculated intensities, and blue lines are the difference between the observed and calculated intensities. Short vertical lines show the positions of Bragg reflections for $TlErSe_2$ and $TlTmSe_2$, as well as for Si (internal standard).

the rhombohedral α-$NaFeO_2$ structure and space group $R\bar{3}m$ (No. 166). Tl^{1+}, R^{3+} (R: rare earth), and Se^{2-} atoms occupy the Wyckoff positions (atomic coordinates) 3*b* (0, 0, 0.5), 3*a* (0, 0, 0), and 6*c* (0, 0, z), respectively. Therefore, during the refinement analysis, only the z coordinate of the Se atom was refined. The obtained lattice parameters and the reliability factors of both compounds are shown in Table I. They are in good agreement with the values reported by Duczmal and Pawlak [27,45] but quite different from the ones reported by Kabré *et al.* [25]. This difference may be related to the fact that in Ref. [25] the lattice parameter determination was done over only 12 diffraction peaks. The lattice parameters of the isostructural and nonmagnetic reference $TlLuSe_2$ are $a = 4.0656(7)$ Å, $c = 23.1769(4)$ Å, and $V = 331.77(1)$ Å^3. The isotropic thermal displacement parameters B_{eq} were kept fixed at 1.0 Å^2, and the site occupancies were also fixed to 1.0 in the refinements; the structural parameters of the Rietveld fits are summarized in Table I. Furthermore, energy dispersive x-ray analysis and inductively coupled plasma optical emission spectroscopy (ICP-OES) measurements of the powder samples of $TlErSe_2$ and $TlTmSe_2$ confirm the homogeneity and stoichiometric composition of the delafossite compounds.

The refined crystal structures of $TlErSe_2$ and $TlTmSe_2$ are shown in Fig. 2, in which the stacked layered $ErSe_6$ and $TmSe_6$ octahedra are arranged in an *ABC* sequence and separated by 7.718 and 7.7116 Å, respectively. The bond lengths and angles of the slightly distorted $ErSe_6$ and $TmSe_6$ octahedra together with a single layer of Er or Tm atoms ordered in a perfect triangular lattice are also indicated.

Figure 3(a) shows the magnetization of $TlErSe_2$ divided by the applied field M/H as a function of temperature in an external magnetic field of 1 T. The data were fitted with the Curie-Weiss law, i.e., $M/H(T) = C/(T - \Theta_{CW})$, for temperatures above 200 K. The corresponding fitting yields an effective moment of $\mu_{eff} = 9.6 \pm 0.2\mu_B$/Er and a Curie-Weiss temperature of $\Theta_{CW} = -(7 \pm 1)$ K. The effective moment is in good agreement with the expected value for a trivalent free Er ion of $\mu_{eff} = 9.58\mu_B$ [46]. Similar results were found in other Er-based delafossites such as $NaErSe_2$ and $KErSe_2$, where $\mu_{eff} = 9.5\mu_B$ was reported for both compounds [47]. The negative Θ_{CW} indicates sizable antiferromagnetic correlations between the Er^{3+} ions. Down to the lowest measured temperature of 1.8 K no sign of ordering is observed, resulting in a minimal frustration factor $f = |\Theta_{CW}/T_N|$ [48] of ∼3.9. The inset shows M/H as a function of the temperature for applied fields $\geqslant 2$ T and its first derivative. dM/dT reveals a minimum at 3.2 K and 2 T that shifts toward higher temperatures and broadens with increasing applied field. This minimum is taken as an indication of the gradual field polarization (see Fig. 11 below). This observation agrees well with the field-dependent measurement of the magnetization [Fig. 4(a)]. At low temperatures, the moment first steeply increases with increasing field and then slowly tapers off, becoming almost linear for applied fields greater than ∼10 T, finally reaching ∼6.5μ_B/Er at 14 T and 2 K.

Figure 3(b) shows the temperature dependence of the magnetization divided by the applied magnetic field for $TlTmSe_2$.

TABLE I. Rietveld results for structural parameters, atomic coordinates (x, y, z), and equivalent isotropic displacement parameters B_{eq}. Residual factors are $R_p(\%) = 7.31$, $R_{wp}(\%) = 9.71$, and $R_{exp}(\%) = 4.82$, and the goodness of fit (GOF) is 2.02 for $TlTmSe_2$; $R_p(\%) = 5.40$, $R_{wp}(\%) = 7.10$, and $R_{exp}(\%) = 4.89$, and the GOF is 1.45 for $TlErSe_2$.

Lattice parameters	Atom	Wyckoff position	x	y	z	Occupancy	B_{eq} (Å^2)
$a = 4.1070(4)$ Å	Er	3*a*	0	0	0	1.0	1.0
$c = 23.147(1)$ Å	Tl	3*b*	0	0	1/2	1.0	1.0
$V = 338.13(7)$ Å^3	Se	6*c*	0	0	0.267(1)	1.0	1.0
$a = 4.0916(1)$ Å	Tm	3*a*	0	0	0	1.0	1.0
$c = 23.1483(2)$ Å	Tl	3*b*	0	0	1/2	1.0	1.0
$V = 335.602(6)$ Å^3	Se	6*c*	0	0	0.2657(5)	1.0	1.0

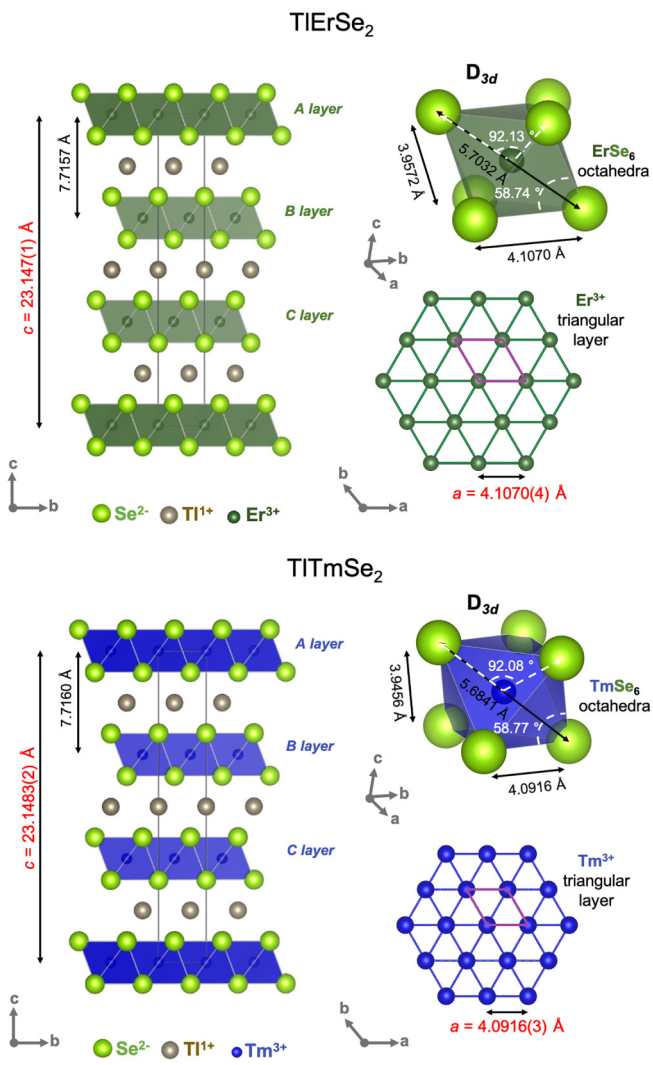


FIG. 2. Refined crystal structures of $TlErSe_2$ and $TlTmSe_2$ with space group $R\bar{3}m$. The $ErSe_6$ and $TmSe_6$ distorted octahedra with the D_{3d} structure and a diagram of a single perfect triangular layer of Er^{3+} and Tm^{3+} ions (viewed along the c axis) are also shown. The unit cells are indicated with solid purple lines. Tl^{1+}, Er^{3+} (Tm^{3+}), and Se^{2-} atoms are shown in brown, dark green (blue), and light green, respectively. Illustrations were generated with VESTA [49].

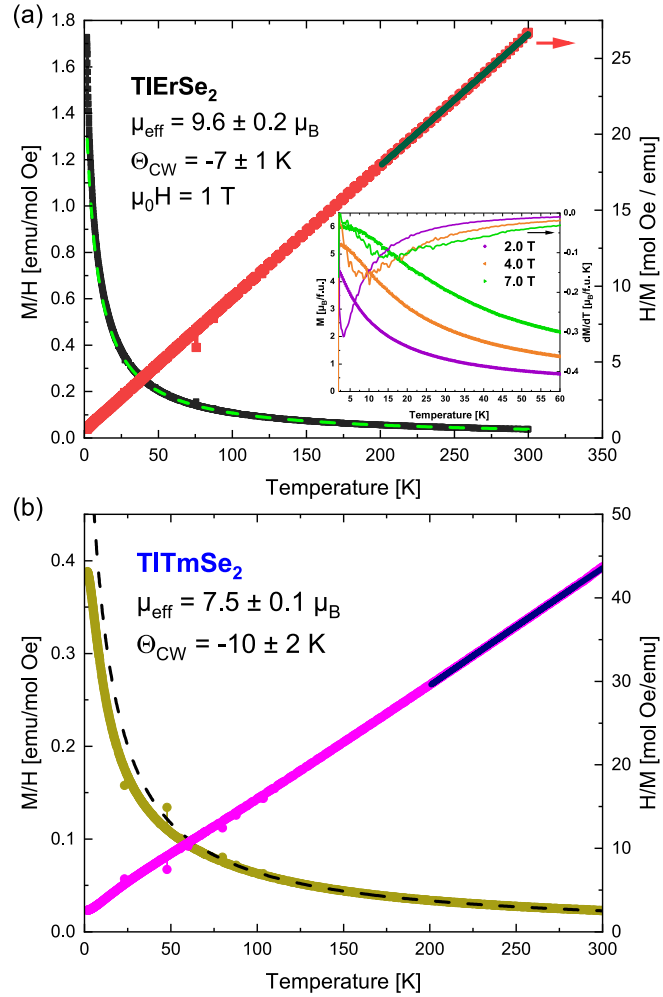


FIG. 3. (a) Temperature dependence of the magnetization of $TlErSe_2$ divided by the applied field M/H and its inverse. The inset shows the temperature dependence of the magnetization and its first derivative of $TlErSe_2$ for applied fields of 2, 4, and 7 T. (b) M/H and its inverse for $TlTmSe_2$ as a function of temperature measured at 1 T. The solid lines correspond to a Curie-Weiss fit for temperatures above 200 K, and the dashed lines correpond to an extrapolation of the resulting Curie-Weiss fit down to the lowest temperature.

The data show no evidence of a magnetic transition in $TlTmSe_2$ down to 1.8 K. M/H follows a Curie-Weiss law above 200 K. The fit yields an effective moment of $\mu_{\text{eff}} = (7.5 \pm 0.1)\mu_B/\text{Tm}$ and a Curie-Weiss temperature of $\Theta_{\text{CW}} = (-10 \pm 2)$ K. The obtained effective moment is in good agreement with the theoretical moment of the free Tm^{3+} ion ($7.57\,\mu_B$) [46]. Θ_{CW} indicates sizable antiferromagnetic correlations. The resulting frustration factor is at least $f \gtrsim 5$. At around ∼100 K the magnetic behavior starts to deviate from the Curie-Weiss law, with the observed magnetization being smaller than the free-ion value, indicating a reduction of the Curie constant C as a function of temperature.

Isothermal magnetization data of $TlTmSe_2$ collected at various temperatures are plotted in Fig. 4(b). The low-temperature data show a steep increase of the magnetic moment over the first 3 T up to $\sim 2\mu_B$/f.u., which then slowly transitions into a linear behavior for fields greater than ∼12 T. The linear behavior above ∼12 T may at least partly be attributed to a temperature-independent Van Vleck contribution stemming from excitations to a higher CEF level.

It should be noted, however, that the measured samples are polycrystalline and thus the observed finite linear slope at high field may originate not purely from a Van Vleck contribution but from the polycrystalline average. Rare-earth magnets in general and, more specifically, rare-earth-based delafossites commonly display a large g factor anisotropy [47,50–52]. The presented data are a powder average and thus an admixture of the magnetic easy and hard directions. The saturation field of the latter might exceed our experimental accessible range and hence results in the observation of a finite slope for large applied fields. Thus, we refrain from fitting the field-dependent magnetization data.

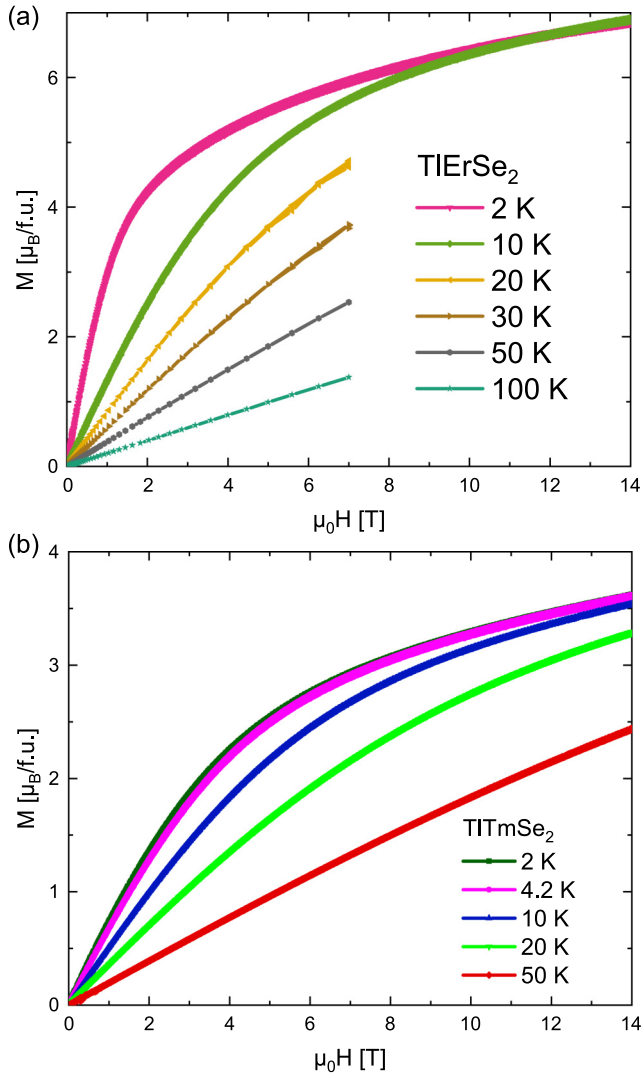


FIG. 4. Field dependence of the magnetic moment per formula unit of (a) $TlErSe_2$ and (b) $TlTmSe_2$ for various temperatures.

To further explore the low-temperature magnetism of the two samples we extracted the magnetic contribution of the specific heat for various applied fields up to 9 T measured down to 0.36 mK. The phononic contribution was subtracted by Lindemann scaling the specific heat of the nonmagnetic analog $TlLuSe_2$.

$C_{p,\mathrm{mag}}$ of $TlErSe_2$ (Fig. 5) reveals a sharp peak at 420 mK and zero field. This peak is suppressed by applying an external magnetic field until no sharp specific heat peak is observable down to 0.36 K at 0.5 T. It marks the onset of long-range antiferromagnetic order. Besides the sharp main peak, a faint shoulder is observed, which develops into a broad hump (labeled T^*), shifting toward higher temperatures with increasing fields. This broad feature is typical for quasi-two-dimensional (quasi-2D) systems and most likely indicates the onset of 2D correlations. In addition, a second hump at higher temperatures, i.e., around $T \sim 12\,\mathrm{K}$ (T_{CEF}) is observed. This broad feature originates from the population of higher CEF levels. T_{CEF} remains rather stationary for fields up to 4 T. In this field range both humps merge and become indistinguishable. At an applied field of 9 T the combined maximum is shifted to ∼17 K.

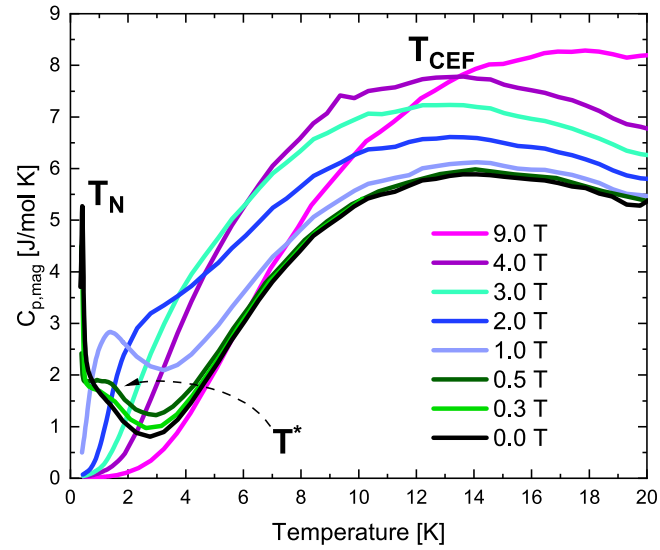


FIG. 5. Magnetic contribution of the specific heat $C_{p,\mathrm{mag}}$ of $TlErSe_2$ as a function of temperature for various magnetic fields. T_N marks the transition temperature, and T^* corresponds to the shoulderlike feature in addition to the broad maximum T_{CEF} from the populated higher CEF level.

The corresponding entropy release ΔS_{mag} is presented in Fig. 6 and shows a steep increase corresponding to the sharp specific heat peak of the magnetic phase transition followed by a leveling-off in the low-temperature regime ($T < 6\,\mathrm{K}$). The plateaulike feature is close to $R\ln(2)$. This is the expected value for a $\tilde{S} = 1/2$ spin system, verifying the ground-state KD. With the transition temperature $T_N = 0.420\,\mathrm{K}$ close to the system's limitation it is not possible to capture the full

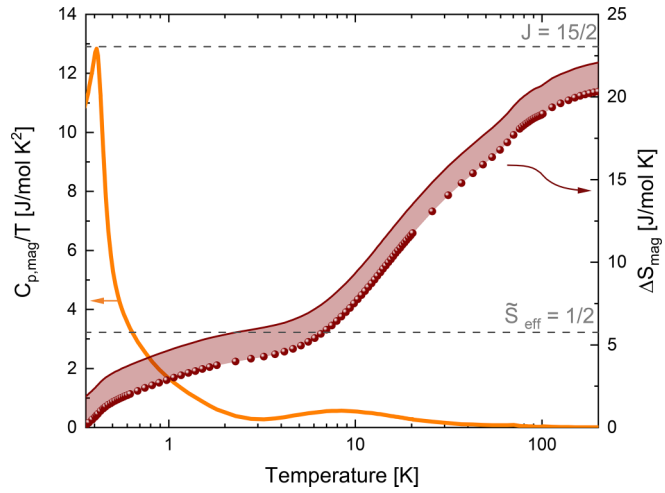


FIG. 6. Magnetic contribution of the specific heat divided by temperature $C_{p,\mathrm{mag}}/T$ of the zero-field measurement (orange solid line, left y axis) and the corresponding integrated magnetic entropy (red dots, right y axis) of $TlErSe_2$. The solid red line indicates an estimate of the entropy which is missing from the temperature range below 0.35 K. The two dashed gray lines mark the expected entropy values for an $\tilde{S} = 1/2$ and $J = 15/2$ state.

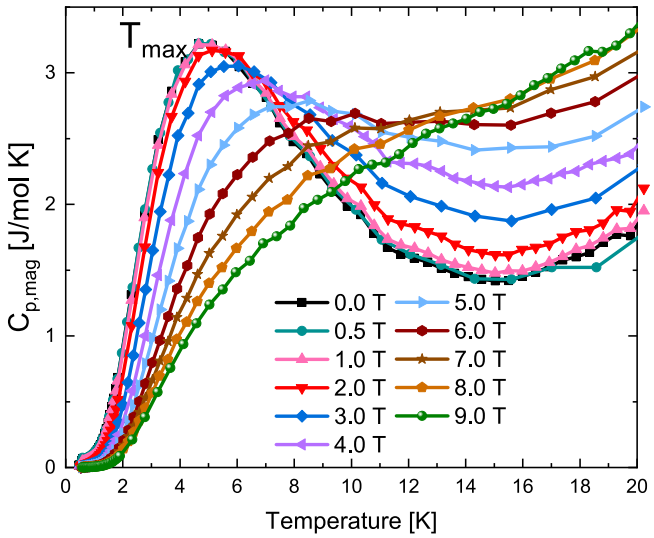


FIG. 7. Magnetic contribution of the specific heat $C_{p,\mathrm{mag}}$ as a function of temperature for $TlTmSe_2$ for various magnetic fields. T_{max} marks the observed broad maximum, which broadens even further for large applied fields.

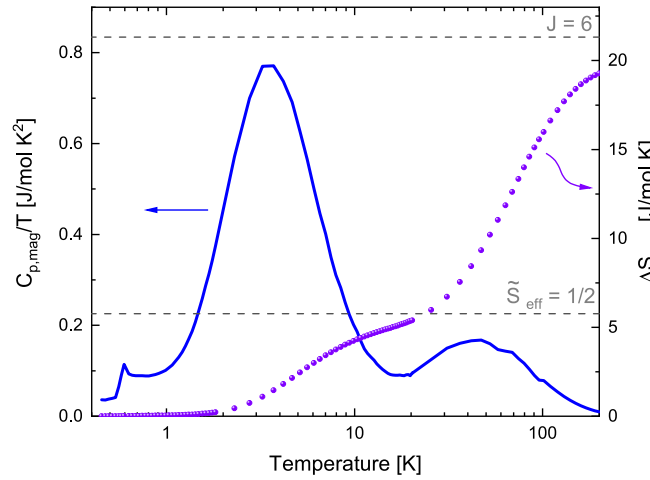


FIG. 8. Magnetic contribution of the specific heat divided by temperature $C_{p,\mathrm{mag}}/T$ of the zero-field measurement (blue solid line, left y axis) and the corresponding integrated magnetic entropy released (purple dots, right y axis) for $TlTmSe_2$. The two dashed gray lines mark the expected entropy values for an effective spin $\tilde{S} = 1/2$ and $J = 6$ state.

peak. Therefore, some of the entropy at low temperatures is not accounted for when integrating over $C_{p,\mathrm{mag}}/T$. A rough estimate of this contribution to S_{mag} is given by the red shaded area above the data points. $C_{p,\mathrm{mag}}$ was fitted with $C_{p,\mathrm{mag}} \propto T^3$, which is expected for an antiferromagnet close to T_N [53]. Above 6 K the released entropy increases steadily approaching $R \ln [2(15/2) + 1]$, the value expected for a free Er^{3+} ion.

The magnetic contribution of the specific heat measurement of $TlTmSe_2$ as a function of temperature is displayed in Fig. 7 for various applied magnetic fields. Throughout the whole temperature range, no sharp anomaly, apart from a small measurement artifact around ∼0.55 K [54], is observed, suggesting the absence of a spontaneous long-range magnetic order phase transition down to ∼0.5 K. The magnetic contribution of the specific heat exhibits a broad maximum at $T_{\mathrm{max}} = 5$ K for magnetic fields below 2 T. With increasing field strength the maximum shifts linearly toward higher temperatures and smears out further. Figure 8 shows $C_{p,\mathrm{mag}}/T$ at zero field up to ∼200 K. In the higher-temperature regime, another broad feature T_{CEF} is observed at approximately 45 K. The origin of this bump can be related to the higher crystal electric field levels being populated, which is supported by the released entropy in this temperature regime. The obtained magnetic entropy is also shown in Fig. 8. It experiences a plateaulike feature around $R \ln (2)$, similar to $TlErSe_2$. While this may indicate an $\tilde{S} = 1/2$ regime below ∼20 K, the entropy released for a Schottky-like anomaly originating from two singlet states is expected to yield the same value, as S depends solely on the ratio of degeneracies g_1/g_0 for a two-level system [53]. When we consider the reduction of μ_{eff} for low temperatures as well as the CEF calculations presented below, the lowest energy levels are (nonmagnetic) singlet states, and thus, the second scenario is more plausible for the Tm compound. For elevated temperatures, the entropy approaches the expected value for the $J = 6\,4f$ manifold of a free Tm^{3+} ion.

In Fig. 9 the magnetic contribution of the specific heat is fitted with a Schottky approach using three energy levels, E_1, E_2, and E_3; while the first two correspond to the ground and first excited CEF levels, the third accounts for higher CEF levels. For the degeneracy g_i of the levels the best fit was obtained with E_1 and E_2 having the same value and g_3 being twice that value. From this we conclude that the two lowest energy levels are most likely singlet states with an energy gap of 11.8 ± 0.2 K, which is in agreement with the quantum chemical calculations presented below.

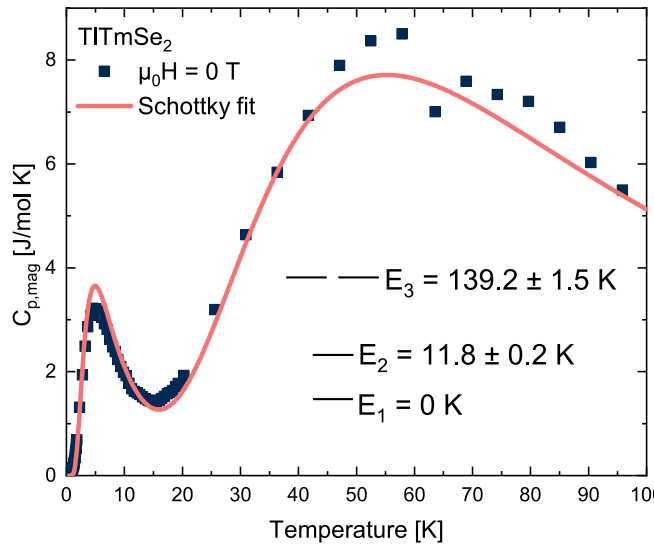


FIG. 9. Magnetic contribution of the specific heat of $TlTmSe_2$ as a function of temperature for zero field. The solid line corresponds to a Schottky fit considering three energy levels [53]. The level scheme is depicted, and the data are best described with a degeneracy ratio of 1 : 1 : 2 for energy levels E_1, E_2, and E_3, respectively.

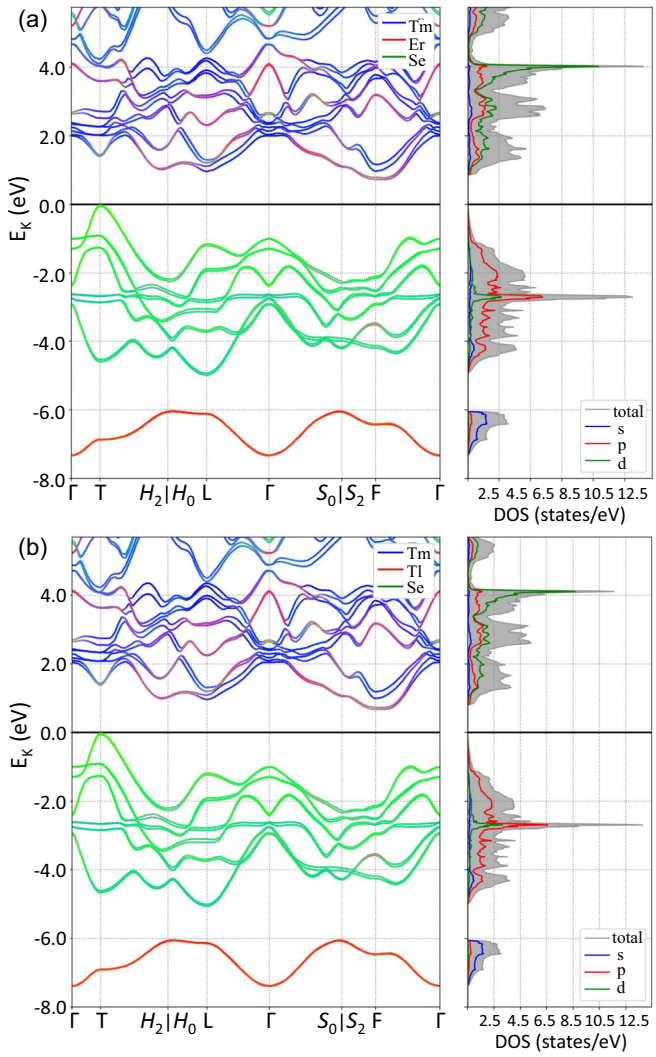


FIG. 10. Band structures and density of states of (a) $TlErSe_2$ and (b) $TlTMSe_2$.

In order to establish a microscopic basis for the different experimentally observed magnetic and thermodynamic properties of the two compounds, we performed density-functional and wave function quantum chemical calculations. These calculations allow us to determine the basic energy scales in the two materials.

In the density-functional computations both materials are insulators. Figures 10(a) and 10(b) show the band structures and density of states (DOS) in $TlErSe_2$ and $TlTmSe_2$, respectively. The calculated band structures show strong similarities, with almost identical dispersions over the Brillouin zone. This is not surprising, as the two compounds are isostructural. The top of the valence bands in both materials consists predominantly of p states of Se. The conduction band electrons originate from both the d-electron orbitals of Er or Tm and the p electrons of Tl. The resulting indirect gap is about 0.74 eV for $TlErSe_2$ and 0.69 eV for $TlTmSe_2$.

For insights into the $4f$ electronic structures and the local CEF splittings we carried out quantum chemical calculations. The low-energy $4f^{11}$ NEVPT2 spectrum of $TlErSe_2$ is defined by a group of eight KDs with relative energies of 0, 6.5, 7.4, 8.7, 11.3, 30.4, 32.4, and 33.4 meV, related to the $J=15/2$ free-ion ground-state term. Other excited SO states require excitation energies of at least 0.75 eV. Notably, the NEVPT2 treatment brings significant corrections to the CASSCF relative energies, an aspect that is detailed in the Appendix (Table III). The lowest excited state lies somewhat lower compared to the case of $4f^{13}$ ions in a similar crystalline environment [21,41].

TABLE II. Low-lying energy gap in different Tm^{3+} compounds.

Compound	Gap in meV (K)	Ref.
$TlTmSe_2$	∼1 (11.8)	This work
$TmMgGaO_4$	0.54 (6.2)	[56]
$TmZn_2GaO_5$	0.15 (1.7)/0.91 (10.6)[a]	[57]
$KTmSe_2$	1.17 (13.6)	[11]
$NaTmSe_2$	1.34 (15.8)	[55]

[a]The first value was obtained from the powder inelastic neutron (IN) scattering data at 5 K, and the second value was obtained from a combination of powder and single-crystal IN data at 5 and 0.05 K, respectively.

The CASSCF (NEVPT2) results seem to slightly underestimate (overestimate) the lowest excitation energy when compared to the increase in magnetic entropy observed in the specific heat. This may be associated with limitations of the perturbational post-CASSCF correlation treatment and of the basis-set optimization.

The low-energy MRCI spectrum for the $TlTmSe_2$ compound is defined by a group of five singlets and four doublets with relative energies of 0, 0.8, 3.5, 5.1, 9.0, 12.9, 18.7, 19.1, and 21.7 meV, related to the $J=6$ free-ion ground-state term. Other excited SO states are located above 0.95 eV. The MRCI treatment brings significant corrections to the CASSCF excitation energies, as presented in Table IV. In other $4f^{12}$ triangular-lattice compounds, e.g., $KTmSe_2$ [11] and $NaTmTe_2$ [55], the experimentally determined first excited state is at 1.2 and 2.9 meV, respectively. This gap (0.8 meV in $TlTmSe_2$ at the MRCI level, somewhat lower than in $KTmSe_2$ [11] and $NaTmTe_2$ [55]) is defined by two singlet states that can be mapped onto a pseudodoublet on-site ground state [6]. One effect we checked computationally in $TlTmSe_2$ was the dependence of the $4f^{12}$ multiplet

TABLE III. Low-energy $4f$-site multiplet structure in $TlErSe_2$ ($J=15/2$-like levels); relative energies of the lowest eight KDs (meV) are given. All possible states derived from the $4f^{11}$ configuration entered the SO treatment.

Level	CASSCF+SOC	NEVPT2+SOC
1	0.0	0.0
2	0.9	6.5
3	5.0	7.4
4	6.0	8.7
5	7.0	11.3
6	18.3	30.4
7	20.8	32.4
8	22.3	33.4

TABLE IV. Low-energy $4f$-site multiplet structure in $TlTmSe_2$ ($J = 6$-like levels); relative energies are in meV. The lowest 11 spin triplets and nine spin singlets derived from the $4f^{12}$ configuration entered the SO treatment. The levels joined by brackets are doublets not split by the crystal field.

Level	CASSCF+SOC	MRCI+SOC
1	0.0	0.0
2	1.2	0.8
3 ⎫	1.9	3.5
4 ⎭		
5 ⎫	3.3	5.1
6 ⎭		
7	6.8	9.0
8	10.2	12.9
9	14.0	18.7
10⎫	14.7	19.1
11⎭		
12⎫	17.2	21.7
13⎭		

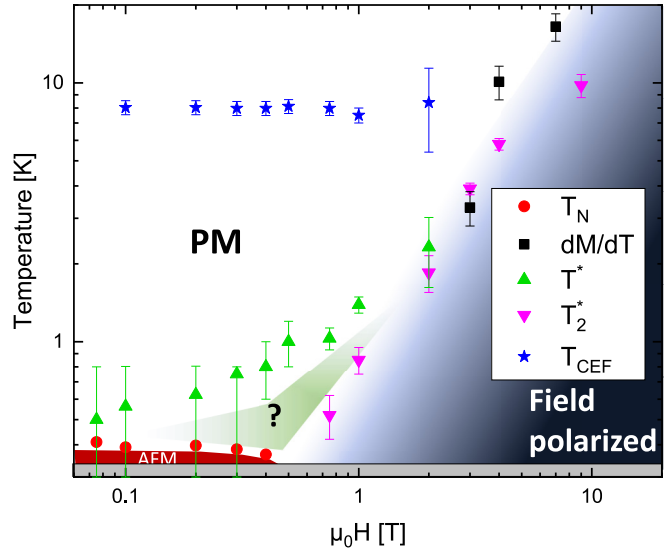


FIG. 11. Field-temperature phase diagram of $TlErSe_2$ on a log-log scale. Marked are T_N (red circles) corresponding to the sharp peak and the shoulder (light green triangles), which develops into a broad bump (pink triangles) observed in $C_{p,\mathrm{mag}}$, as well as the onset of saturation as measured by high field susceptibility (black squares); for more information see the text. The colored areas are meant to guide the eye. The gray shaded area below marks the temperature limit of the device.

structure on the amount of trigonal distortion. Interestingly, we found that the sequence of low-lying excited states can be modified by reducing the amount of trigonal compression: With the squeezing of the octahedral cage removed, this sequence changes from singlet-singlet-doublet-etc. (i.e., from the pseudodoublet ground-state magnetic picture) to singlet-doublet-singlet-etc. when removing trigonal compression, which, in principle, leaves room for fine tuning of (and even for switching the nature of) magnetic ground states in this family of compounds. These findings expand the excitonic-magnetism phenomenology discussed by Khaliullin in the context of d^4 SO-coupled systems [58].

IV. DISCUSSION AND SUMMARY

Our results show that $TlErSe_2$ is an example of a magnetically long-range ordered triangular-lattice antiferromagnet made of $\tilde{S} = 1/2$ KD moments. This places it in the class of ordered rare-earth delafossites such as $NaErSe_2$ [47], $NaErS_2$ [59], $KCeS_2$ [51,60], $KErSe_2$ [47,61], and $KYbSe_2$ [62], contrasting with putative candidates like $NaYbSe_2$ [17,23], $NaYbO_2$ [63], $KYbS_2$ [64], and $CsYbSe_2$ [65]. While both kinds of behaviors are observed within the delafossite family a clear tuning parameter remains unclear and under debate. However, it is evident that anisotropic exchange and crystal field effects likely play a significant role.

For similar Er^{3+}-based triangular-lattice compounds both easy plane (XY) anisotropy ([66], $K_3Er(VO_4)_2$ [67], $NaErSe_2$ [47], $CsErSe_2$ [52]) and Ising anisotropy ($Ba_3ErB_9O_{18}$ [68]) were reported. This highlighs the sensitivity of the magnetic ground state to the m_J composition of the ground-state doublet, i.e., to the CEF environment, motivating further studies on single crystals.

In $TlErSe_2$, the low ordering temperature, together with the large total angular momentum of the $J = 15/2$ manifold, suggests that dipolar interactions may contribute significantly to stabilizing long-range order. Within this scenario, a stripelike magnetic structure with the moments pointing along the Er-Er bond axis is plausible; however, the exact magnetic structure remains to be determined.

In addition to the pronounced peak at T_N, a shoulder-like feature was observed evolving into a broad hump at larger fields (see Fig. 11). Due to the delafossite crystal structure, i.e., stacked rare-earth ion triangular layers well separated by A^+ spacer layers, the hierarchy of the magnetic couplings $\mathcal{J}$ closely resembles quasi-2D systems with $\mathcal{J}_{\mathrm{intralayer}} \gg \mathcal{J}_{\mathrm{interlayer}}$. Here, these broad features appearing just before a magnetically ordered state forms correspond to 2D correlations [69].

While the work by Liu *et al.* [70] proposed numerous ordered states for non-KDs on a triangular lattice, in contrast to $TlErSe_2$, no sign indicating long-range magnetic order was found in $TlTmSe_2$ down to 360 mK. These findings are in line with reports on related compounds such as $KTmSe_2$ [11], $NaTmSe_2$ [71], and $LiTmSe_2$ [71]. Our quantum chemical calculations suggest a sizable energy gap of $\sim$1 meV between the two lowest singlet states. This is in good agreement with the energy scale extracted from a two-level Schottky analysis of the specific heat, yielding $\Delta \approx 11.8$ K (≈ 1 meV) with a degeneracy ratio of 1 : 1. With reports of "hidden" or multipolar order in compounds like $TmMgGaO_4$ [7,56] and $TmZn_2GaO_5$ [57], it is interesting to compare the low-energy gapped excitation in other thulium-based transverse field Ising candidates. As summarized in Table II, $TlTmSe_2$ joins this material class as a promising candidate for future work.

In summary, we reported the synthesis of high-quality polycrystalline $TlMSe_2$ (M: Er or Tm) samples. While the erbium compound shows clear signs of long-range antiferromagnetic order below 420 mK, no such signs were found for $TlTmSe_2$. This profound difference in the magnetic

properties is related to the distinct difference in the CEF level structure. For $TlErSe_2$ the $\tilde{S} = 1/2$ KD moments of the Er^{3+} ions most likely imply contributions of large $|m_J\rangle$, which results in a sizable dipolar coupling, strong enough to stabilize long-range order in the ^{3}He temperature range. On the other hand, the absence of long-range order in $TlTmSe_2$ is primarily attributed to a nonmagnetic singlet ground state. However, in related compounds such as $TmMgGaO_4$ [56] and $NaTmSe_2$ [55] hidden multipolar order was reported to arise from strong intersite exchange interactions comparable in energy to the gap of the CEF quasidoublet. The singlet-singlet gap of $TlTmSe_2$ fits well with the reported energy gaps in these compounds; therefore, we cannot entirely rule out a similar scenario for our system.

Interestingly, numerical experiments carried out for the $4f^{12}$ system indicate a high sensitivity to the amount of trigonal compression: If the latter is removed, not only the CEF splittings but also the sequence of low-lying CEF states can be dramatically modified. This calls for special attention when making assignments to the lowest excited states in experimental studies across the $4f^{12}$ AMX_2 family.

ACKNOWLEDGMENTS

We acknowledge financial support from the German Research Foundation (DFG) within the SFB 1143 Correlated Magnetism From Frustration to Topology, Project ID No. 247310070 (Projects No. B01, No. B03, and No. A05) and Project No. 390858490 (Würzburg-Dresden Cluster of Excellence on Complexity and Topology in Quantum Matter – ct.qmat, EXC 2147) We appreciate the ICP-OES measurements by Dr. Gudrun Auffermann (MPI-CPfS Dresden). D.V.E. and A.N. thank M. Richter for discussions and U. Nitzsche for technical support and acknowledge financial support from the DFG, Projects No. 529677299 and No. 455319354. P.B. and L.H. thank T. Petersen for discussions, U. Nitzsche for technical support, and the DFG (Project No. 441216021) for financial support.

DATA AVAILABILITY

There are no publicly available research data or software supporting this manuscript. Requests for further information or data should be sent to the authors.

APPENDIX: FURTHER QUANTUM CHEMICAL CALCULATIONS

We employed the SARC2-DKH-QZVP basis set (BS) for the central Er^{3+} $4f^{11}$ ion [72] and all-electron relativistic BSs of triple-ζ quality for the Se ligands [73] of the $ErSe_6$ octahedron (Tables III and IV); within the buffer cationic region between the reference $ErSe_6$ octahedron and the point-charge matrix, large-core pseudopotentials were utilized for the 6 Er^{3+} [74] and 12 Tl^+ [75] species.

TABLE V. Low-energy $4f$-site multiplet structure (meV) in $TlErSe_2$ at the NEVPT2+SOC level and dependence on the number of states considered in the SO computations. Q and D stand for quartet and doublet spin multiplicities, respectively.

Level	(30 Q + 43 D)[a]	(35 Q + 112 D)
1	0.0	0.0
2	6.5	6.5
3	7.4	7.4
4	8.6	8.7
5	11.2	11.3
6	30.4	30.4
7	32.4	32.4
8	33.4	33.4

[a]Orbitals as employed in the adjacent column were used.

Negligible changes in the relative energies were observed if only 30 spin quartets and 43 spin doublets instead of all possible states associated with the Er^{3+} $4f^{11}$ configuration were considered in the quantum chemical calculations (see Table V).

For the central Tm^{3+} $4f^{12}$ ion energy-consistent quasirelativistic pseudopotentials (ECP28MWB) [74] and Gaussian-type valence BSs of effective quadruple-ζ quality [76,77] were employed, whereas we used relativistic pseudopotentials (ECP46MDF) [78] along with $(6s6p)/[4s4p]$ valence BSs for the six Se ligands of the central $TmSe_6$ octahedron (Table VI).

Large-core pseudopotentials including the $4f$ subshell in the core (ECP58MWB) [79,80] were adopted for the six adjacent Tm sites, along with $(4s3p)/[2s1p]$ valence BSs. We considered large-core pseudopotentials for the 12 Tl nearest neighbors (ECP78MWB) [75] with $(4s3p)/[2s1p]$ valence BSs.

TABLE VI. Low-energy $4f$-site multiplet structure (meV) in $TlTmSe_2$ at the CASSCF+SOC level and dependence on the number of states considered in the SO computations (relative energies are in meV). T and S stand for triplet and singlet spin multiplicities, respectively.

Level	(11 T + 9 S)[a]	(21 T + 28 S)
1	0.0	0.0
2	1.2	1.2
3 ⎫	1.9	1.9
4 ⎭		
5 ⎫	3.3	3.2
6 ⎭		
7	6.8	6.6
8	10.2	10.0
9	14.0	13.8
10⎫	14.7	14.4
11⎭		
12⎫	17.2	16.9
13⎭		

[a]Orbitals as employed in the adjacent column were used.

[1] I. Kimchi and A. Vishwanath, Kitaev-Heisenberg models for iridates on the triangular, hyperkagome, kagome, fcc, and pyrochlore lattices, Phys. Rev. B **89**, 014414 (2014).

[2] C. Kim, S. Kim, P. Park, T. Kim, J. Jeong, S. Ohira-Kawamura, N. Murai, K. Nakajima, A. L. Chernyshev, M. Mourigal, S.-J. Kim, and J.-G. Park, Bond-dependent anisotropy and magnon decay in cobalt-based Kitaev triangular antiferromagnet, Nat. Phys. **19**, 1624 (2023).

[3] P. Bhattacharyya, N. A. Bogdanov, S. Nishimoto, S. D. Wilson, and L. Hozoi, $NaRuO_2$: Kitaev-Heisenberg exchange in triangular-lattice setting, npj Quantum Mater. **8**, 52 (2023).

[4] T. Xie, S. Gozel, J. Xing, N. Zhao, S. M. Avdoshenko, L. Wu, A. S. Sefat, A. L. Chernyshev, A. M. Läuchli, A. Podlesnyak, and S. E. Nikitin, Quantum spin dynamics due to strong Kitaev interactions in the triangular-lattice antiferromagnet $CsCeSe_2$, Phys. Rev. Lett. **133**, 096703 (2024).

[5] B. R. Ortiz, M. M. Bordelon, P. Bhattacharyya, G. Pokharel, P. M. Sarte, L. Posthuma, T. Petersen, M. S. Eldeeb, G. E. Granroth, C. R. Dela Cruz, S. Calder, D. L. Abernathy, L. Hozoi, and S. D. Wilson, Electronic and structural properties of $RbCeX_2$ (X_2 : O_2, S_2, SeS, Se_2, TeSe, Te_2), Phys. Rev. Mater. **6**, 084402 (2022).

[6] G. Chen, Intrinsic transverse field in frustrated quantum Ising magnets: Physical origin and quantum effects, Phys. Rev. Res. **1**, 033141 (2019).

[7] Y. Shen, C. Liu, Y. Qin, S. Shen, Y.-D. Li, R. Bewley, A. Schneidewind, G. Chen, and J. Zhao, Intertwined dipolar and multipolar order in the triangular-lattice magnet $TmMgGaO_4$, Nat. Commun. **10**, 4530 (2019).

[8] Z. Dun, M. Daum, R. Baral, H. E. Fischer, H. Cao, Y. Liu, M. B. Stone, J. A. Rodriguez-Rivera, E. S. Choi, Q. Huang, H. Zhou, M. Mourigal, and B. A. Frandsen, Neutron scattering investigation of proposed Kosterlitz-Thouless transitions in the triangular-lattice Ising antiferromagnet $TmMgGaO_4$, Phys. Rev. B **103**, 064424 (2021).

[9] Z. Hu, Z. Ma, Y.-D. Liao, H. Li, C. Ma, Y. Cui, Y. Shangguan, Z. Huang, Y. Qi, W. Li, Z. Y. Meng, J. Wen, and W. Yu, Evidence of the Berezinskii-Kosterlitz-Thouless phase in a frustrated magnet, Nat. Commun. **11**, 5631 (2020).

[10] C. Liu, C.-J. Huang, and G. Chen, Intrinsic quantum Ising model on a triangular lattice magnet $TmMgGaO_4$, Phys. Rev. Res. **2**, 043013 (2020).

[11] S. Zheng, H. Wo, Y. Gu, R. L. Luo, Y. Gu, Y. Zhu, P. Steffens, M. Boehm, Q. Wang, G. Chen, and J. Zhao, Exchange-renormalized crystal field excitations in the quantum Ising magnet $KTmSe_2$, Phys. Rev. B **108**, 054435 (2023).

[12] Y. D. Liao, H. Li, Z. Yan, H.-T. Wei, W. Li, Y. Qi, and Z. Y. Meng, Phase diagram of the quantum Ising model on a triangular lattice under external field, Phys. Rev. B **103**, 104416 (2021).

[13] S. V. Isakov and R. Moessner, Interplay of quantum and thermal fluctuations in a frustrated magnet, Phys. Rev. B **68**, 104409 (2003).

[14] M. Baenitz, P. Schlender, J. Sichelschmidt, Y. A. Onykiienko, Z. Zangeneh, K. M. Ranjith, R. Sarkar, L. Hozoi, H. C. Walker, J.-C. Orain, H. Yasuoka, J. van den Brink, H. H. Klauss, D. S. Inosov, and T. Doert, $NaYbS_2$: A planar spin-$\frac{1}{2}$ triangular-lattice magnet and putative spin liquid, Phys. Rev. B **98**, 220409(R) (2018).

[15] K. M. Ranjith, D. Dmytriieva, S. Khim, J. Sichelschmidt, S. Luther, D. Ehlers, H. Yasuoka, J. Wosnitza, A. A. Tsirlin, H. Kühne, and M. Baenitz, Field-induced instability of the quantum spin liquid ground state in the $J_{\text{eff}} = \frac{1}{2}$ triangular-lattice compound $NaYbO_2$, Phys. Rev. B **99**, 180401(R) (2019).

[16] J. Sichelschmidt, P. Schlender, B. Schmidt, M. Baenitz, and T. Doert, Electron spin resonance on the spin-1/2 triangular magnet $NaYbS_2$, J. Phys.: Condens. Matter **31**, 205601 (2019).

[17] K. M. Ranjith, S. Luther, T. Reimann, B. Schmidt, P. Schlender, J. Sichelschmidt, H. Yasuoka, A. M. Strydom, Y. Skourski, J. Wosnitza, H. Kühne, T. Doert, and M. Baenitz, Anisotropic field-induced ordering in the triangular-lattice quantum spin liquid $NaYbSe_2$, Phys. Rev. B **100**, 224417 (2019).

[18] L. Ding, P. Manuel, S. Bachus, F. Grußler, P. Gegenwart, J. Singleton, R. D. Johnson, H. C. Walker, D. T. Adroja, A. D. Hillier, and A. A. Tsirlin, Gapless spin-liquid state in the structurally disorder-free triangular antiferromagnet $NaYbO_2$, Phys. Rev. B **100**, 144432 (2019).

[19] M. M. Bordelon *et al.*, Field-tunable quantum disordered ground state in the triangular-lattice antiferromagnet $NaYbO_2$, Nat. Phys. **15**, 1058 (2019).

[20] M. M. Bordelon, C. Liu, L. Posthuma, P. M. Sarte, N. P. Butch, D. M. Pajerowski, A. Banerjee, L. Balents, and S. D. Wilson, Spin excitations in the frustrated triangular lattice antiferromagnet $NaYbO_2$, Phys. Rev. B **101**, 224427 (2020).

[21] Z. Zhang, X. Ma, J. Li, G. Wang, D. T. Adroja, T. P. Perring, W. Liu, F. Jin, J. Ji, Y. Wang, Y. Kamiya, X. Wang, J. Ma, and Q. Zhang, Crystalline electric field excitations in the quantum spin liquid candidate $NaYbSe_2$, Phys. Rev. B **103**, 035144 (2021).

[22] P.-L. Dai *et al.*, Spinon Fermi surface spin liquid in a triangular lattice antiferromagnet $NaYbSe_2$, Phys. Rev. X **11**, 021044 (2021).

[23] W. Liu, Z. Zhang, J. Ji, Y. Liu, J. Li, X. Wang, H. Lei, G. Chen, and Q. Zhang, Rare-earth chalcogenides: A large family of triangular lattice spin liquid candidates, Chinese Phys. Lett. **35**, 117501 (2018).

[24] T. Fujii, M. Pillaca, F. Bärtl, J. Sichelschmidt, S. Luther, H. Rosner, A. M. Strydom, J. Wosnitza, H. Kühne, T. Doert, and M. Baenitz, $TlYbSe_2$ as a member of the $J = \frac{1}{2}$ triangular-lattice Yb delafossite family: From spin liquid to field-induced magnetic order, Phys. Rev. B **112**, 024426 (2025).

[25] S. Kabré, M. Julien-Pouzol, and M. Guittard, Étude cristallographique des combinaisons ternaires formées par le thallium, les terres rares et le soufre, le sélénium ou le tellure, le long des binaires TL2X−L2X3, Bull. Soc. Chim. Fr. Part I **9-10**, 1881 (1974).

[26] M. Duczmal and L. Pawlak, Magnetic properties of $TiLnS_2$ compounds (Ln Nd, Gd, Dy, Er and Yb), J. Alloys Compd. **209**, 271 (1994).

[27] M. Duczmal and L. Pawlak, Magnetic and structural characterization of $TlLnSe_2$ compounds (Ln Nd to Yb), J. Alloys Compd. **225**, 181 (1995).

[28] T. Ferreira, J. Xing, L. D. Sanjeewa, and A. S. Sefat, Frustrated magnetism in triangular lattice $TlYbS_2$ crystals grown via molten flux, Front. Chem. **8**, 127 (2020).

[29] A. A. Coelho, *TOPAS* and *TOPAS-Academic*: An optimization program integrating computer algebra and crystallographic objects written in C + +, J. Appl. Crystallogr. **51**, 210 (2018).

[30] A. A. Coelho, TOPAS ACADEMIC v4.1 technical reference, Coelho Software, Brisbane, Australia, 2020.

[31] G. Kresse and D. Joubert, From ultrasoft pseudopotentials to the projector augmented-wave method, Phys. Rev. B **59**, 1758 (1999).

[32] G. Kresse and J. Furthmüller, Efficient iterative schemes for *ab initio* total-energy calculations using a plane-wave basis set, Phys. Rev. B **54**, 11169 (1996).

[33] G. Kresse and J. Hafner, *Ab initio* molecular dynamics for open-shell transition metals, Phys. Rev. B **48**, 13115 (1993).

[34] S. P. Ong, W. D. Richards, A. Jain, G. Hautier, M. Kocher, S. Cholia, D. Gunter, V. L. Chevrier, K. A. Persson, and G. Ceder, Python materials genomics (pymatgen): A robust, open-source python library for materials analysis, Comput. Mater. Sci. **68**, 314 (2013).

[35] F. Neese, Software update: The ORCA program system—Version 5.0, Wiley Interdiscip. Rev.: Comput. Mol. Sci. **12**, e1606 (2022).

[36] F. Neese, F. Wennmohs, U. Becker, and C. Riplinger, The ORCA quantum chemistry program package, J. Chem. Phys. **152**, 224108 (2020).

[37] H.-J. Werner, P. J. Knowles, G. Knizia, F. R. Manby, and M. Schütz, Molpro: A general-purpose quantum chemistry program package, Wiley Interdiscip. Rev.: Comput. Mol. Sci. **2**, 242 (2012).

[38] M. Klintenberg, S. Derenzo, and M. Weber, Accurate crystal fields for embedded cluster calculations, Comput. Phys. Commun. **131**, 120 (2000).

[39] S. E. Derenzo, M. K. Klintenberg, and M. J. Weber, Determining point charge arrays that produce accurate ionic crystal fields for atomic cluster calculations, J. Chem. Phys. **112**, 2074 (2000).

[40] P. Bhattacharyya, U. K. Rößler, and L. Hozoi, Crystal-field effects competing with spin-orbit interactions in $NaCeO_2$, Phys. Rev. B **105**, 115136 (2022).

[41] P. Bhattacharyya and L. Hozoi, Yb^{3+} f-f excitations in $NaYbSe_2$: Benchmarking embedded-cluster quantum chemical schemes for $4f$ insulators, Phys. Rev. B **105**, 235117 (2022).

[42] T. Helgaker, P. Jørgensen, and J. Olsen, *Molecular Electronic Structure Theory* (Wiley, Chichester, UK, 2000).

[43] P. J. Knowles and H.-J. Werner, Internally contracted multiconfiguration-reference configuration interaction calculations for excited states, Theor. Chim. Acta **84**, 95 (1992).

[44] C. Angeli, R. Cimiraglia, S. Evangelisti, T. Leininger, and J.-P. Malrieu, Introduction of n -electron valence states for multireference perturbation theory, J. Chem. Phys. **114**, 10252 (2001).

[45] M. Duczmal, Struktura, Właściwości magnetyczne i pole krystaliczne w potrójnych chalkogenkach lantanowców i talu $TlIn\mathit{X}_2$ (X = S, Se lub Te), Thesis, Oficyna Wydawnicza Politechniki Wrocławskiej, Wrocław, 2003.

[46] N. W. Ashcroft and N. D. Mermin, *Solid State Physics* (Holt-Saunders, Philadelphia, 1976).

[47] J. Xing, L. D. Sanjeewa, J. Kim, W. R. Meier, A. F. May, Q. Zheng, R. Custelcean, G. R. Stewart, and A. S. Sefat, Synthesis, magnetization, and heat capacity of triangular lattice materials $NaErSe_2$ and $KErSe_2$, Phys. Rev. Mater. **3**, 114413 (2019).

[48] A. P. Ramirez, G. P. Espinosa, and A. S. Cooper, Strong frustration and dilution-enhanced order in a quasi-2D spin glass, Phys. Rev. Lett. **64**, 2070 (1990).

[49] K. Momma and F. Izumi, *VESTA 3* for three-dimensional visualization of crystal, volumetric and morphology data, J. Appl. Crystallogr. **44**, 1272 (2011).

[50] B. Schmidt, J. Sichelschmidt, K. M. Ranjith, T. Doert, and M. Baenitz, Yb delafossites: Unique exchange frustration of $4f$ spin-$\frac{1}{2}$ moments on a perfect triangular lattice, Phys. Rev. B **103**, 214445 (2021).

[51] G. Bastien *et al.*, Long-range magnetic order in the $\tilde{S} = 1/2$ triangular lattice antiferromagnet $KCeS_2$, SciPost Phys. **9**, 041 (2020).

[52] A. Scheie, V. O. Garlea, L. D. Sanjeewa, J. Xing, and A. S. Sefat, Crystal-field Hamiltonian and anisotropy in $KErSe_2$ and $CsErSe_2$, Phys. Rev. B **101**, 144432 (2020).

[53] E. S. R. Gopal, *Specific Heats at Low Temperatures*, International Cryogenics Monograph Series (Plenum Press, New York, 1966).

[54] The artifact originates from a faulty calibration file of the platform thermometer resistance provided by the manufacturer. The problem was fixed before proceeding with the erbium- and lutetium-based compounds.

[55] S. Zheng, Y. Gu, Y. Gu, Z. Kao, Q. Wang, H. Wo, Y. Zhu, F. Liu, L. Wu, J. Sheng, J. Chang, S. Ohira-Kawamura, N. Murai, C. Niedermayer, D. G. Mazzone, G. Chen, and J. Zhao, Interplay between crystal field and magnetic anisotropy in the triangular-lattice antiferromagnet $NaTmTe_2$, Phys. Rev. B **109**, 075159 (2024).

[56] Y. Li, S. Bachus, H. Deng, W. Schmidt, H. Thoma, V. Hutanu, Y. Tokiwa, A. A. Tsirlin, and P. Gegenwart, Partial up-up-down order with the continuously distributed order parameter in the triangular antiferromagnet $TmMgGaO_4$, Phys. Rev. X **10**, 011007 (2020).

[57] M. Ennis, R. Bag, T. Cookmeyer, M. B. Stone, A. I. Kolesnikov, T. Hong, L. Balents, and S. Haravifard, Emergent hidden multipolar state in the triangular lattice magnet $TmZn_2GaO_5$, arXiv:2503.22009.

[58] G. Khaliullin, Excitonic magnetism in Van Vleck–type d^4 Mott insulators, Phys. Rev. Lett. **111**, 197201 (2013).

[59] S. Gao, F. Xiao, K. Kamazawa, K. Ikeuchi, D. Biner, K. W. Krämer, C. Rüegg, and T.-H. Arima, Crystal electric field excitations in the quantum spin liquid candidate $NaErS_2$, Phys. Rev. B **102**, 024424 (2020).

[60] A. A. Kulbakov, S. M. Avdoshenko, I. Puente-Orench, M. Deeb, M. Doerr, P. Schlender, T. Doert, and D. S. Inosov, Stripe-yz magnetic order in the triangular-lattice antiferromagnet $KCeS_2$, J. Phys.: Condens. Matter **33**, 425802 (2021).

[61] J. Xing, K. M. Taddei, L. D. Sanjeewa, R. S. Fishman, M. Daum, M. Mourigal, C. dela Cruz, and A. S. Sefat, Stripe antiferromagnetic ground state of the ideal triangular lattice compound $KErSe_2$, Phys. Rev. B **103**, 144413 (2021).

[62] A. O. Scheie *et al.*, Witnessing quantum criticality and entanglement in the triangular antiferromagnet $KYbSe_2$ Nat. Phys. **20**, 74 (2024).

[63] J. Wu *et al.*, Magnetic field effects on the quantum spin liquid behaviors of $NaYbS_2$, Quantum Front. **1**, 13 (2022).

[64] R. Iizuka, S. Michimura, R. Numakura, Y. Uwatoko, and M. Kosaka, Single crystal growth and physical properties of Ytterbium Sulfide $KYbS_2$ with triangular lattice, JPS Conf. Proc. **30**, 011097 (2020).

[65] J. Xing, L. D. Sanjeewa, J. Kim, G. R. Stewart, M.-H. Du, F. A. Reboredo, R. Custelcean, and A. S. Sefat, Crystal synthesis and frustrated magnetism in triangular lattice $CsRESe_2$ (RE = La–Lu): Quantum spin liquid candidates $CsCeSe_2$ and $CsYbSe_2$, ACS Mater. Lett. **2**, 71 (2020).

[66] Y. Cai, C. Lygouras, G. Thomas, M. N. Wilson, J. Beare, S. Sharma, C. A. Marjerrison, D. R. Yahne, K. A. Ross, Z. Gong, Y. J. Uemura, H. A. Dabkowska, and G. M. Luke, μSR study of the triangular Ising antiferromagnet $ErMgGaO_4$, Phys. Rev. B **101**, 094432 (2020).

[67] D. R. Yahne, L. D. Sanjeewa, A. S. Sefat, B. S. Stadelman, J. W. Kolis, S. Calder, and K. A. Ross, Pseudospin versus magnetic dipole moment ordering in the isosceles triangular lattice material $K_3Er(VO_4)_2$, Phys. Rev. B **102**, 104423 (2020).

[68] J. Khatua, M. Pregelj, A. Elghandour, Z. Jagličic, R. Klingeler, A. Zorko, and P. Khuntia, Magnetic properties of the triangular-lattice antiferromagnets $Ba_3RB_9O_{18}$ (R = Yb,Er), Phys. Rev. B **106**, 104408 (2022).

[69] P. Sengupta, A. W. Sandvik, and R. R. P. Singh, Specific heat of quasi-two-dimensional antiferromagnetic Heisenberg models with varying interplanar couplings, Phys. Rev. B **68**, 094423 (2003).

[70] C. Liu, Y.-D. Li, and G. Chen, Selective measurements of intertwined multipolar orders: Non-Kramers doublets on a triangular lattice, Phys. Rev. B **98**, 045119 (2018).

[71] M. Boswell, C. Peng, and W. Xie, Magnetic properties of Tm^{3+} in layered triangular lattices, J. Appl. Phys. **137**, 183901 (2025).

[72] D. Aravena, F. Neese, and D. A. Pantazis, Improved segmented all-electron relativistically contracted basis sets for the lanthanides, J. Chem. Theory Comput. **12**, 1148 (2016).

[73] W. A. de Jong, R. J. Harrison, and D. A. Dixon, Parallel Douglas–Kroll energy and gradients in NWChem: Estimating scalar relativistic effects using Douglas–Kroll contracted basis sets, J. Chem. Phys. **114**, 48 (2001).

[74] M. Dolg, H. Stoll, and H. Preuss, Energy-adjusted *ab initio* pseudopotentials for the rare earth elements, J. Chem. Phys. **90**, 1730 (1989).

[75] W. Küchle, M. Dolg, H. Stoll, and H. Preuss, *Ab initio* pseudopotentials for Hg through Rn, Mol. Phys. **74**, 1245 (1991).

[76] X. Cao and M. Dolg, Valence basis sets for relativistic energy-consistent small-core lanthanide pseudopotentials, J. Chem. Phys. **115**, 7348 (2001).

[77] X. Cao and M. Dolg, Segmented contraction scheme for small-core lanthanide pseudopotential basis sets, J. Mol. Struc.: THEOCHEM **581**, 139 (2002).

[78] H. Stoll, B. Metz, and M. Dolg, Relativistic energy-consistent pseudopotentials—Recent developments, J. Comput. Chem. **23**, 767 (2002).

[79] M. Dolg, H. Stoll, A. Savin, and H. Preuss, Energy-adjusted pseudopotentials for the rare earth elements, Theor. Chim. Acta **75**, 173 (1989).

[80] M. Dolg, H. Stoll, and H. Preuss, A combination of quasirelativistic pseudopotential and ligand field calculations for lanthanoid compounds, Theor. Chim. Acta **85**, 441 (1993).